

## Article

# Synthesis of Wrinkled MoS<sub>2</sub> Thin Films Using a Two-Step Method Consisting of Magnetron Sputtering and Sulfurization in a Confined Space

Claudia Mihai <sup>†</sup>, Iosif-Daniel Simandan <sup>†</sup>, Florinel Sava, Angel-Theodor Buruiana , Amelia Elena Bocirnea, Teddy Tite, Mohamed Yassine Zaki  and Alin Velea <sup>\*</sup> 

National Institute of Materials Physics, Atomistilor 405A, 077125 Magurele, Romania; claudia.mihai@infim.ro (C.M.); simandan@infim.ro (I.-D.S.); fsava@infim.ro (F.S.); angel.buruiana@infim.ro (A.-T.B.); amelia.bocirnea@infim.ro (A.E.B.); teddy.tite@infim.ro (T.T.); yassine.zaki@infim.ro (M.Y.Z.)

<sup>\*</sup> Correspondence: alin.velea@infim.ro

<sup>†</sup> These authors contributed equally to this work.

**Abstract:** Considering the increasing need for sustainable and economical energy storage solutions, the integration of layered materials such as MoS<sub>2</sub> into these systems represents an important step toward enhancing energy sustainability and efficiency. Exploring environmentally responsible fabrication techniques, this study assesses wrinkled MoS<sub>2</sub> thin films synthesized from distinct Mo and MoS<sub>2</sub> targets, followed by sulfurization conducted in a graphite box. We utilized magnetron sputtering to deposit precursor Mo and MoS<sub>2</sub> films on Si substrates, achieving thicknesses below 20 nm. This novel approach decreases sulfur by up to tenfold during sulfurization due to the confined space technique, contributing also to avoiding the formation of toxic gases such as SO<sub>2</sub> or the necessity of using H<sub>2</sub>S, aligning with sustainable materials development. Thinner MoS<sub>2</sub> layers were obtained post-sulfurization from the MoS<sub>2</sub> precursors, as shown by X-ray reflectometry. Raman spectroscopy and grazing X-ray diffraction analyses confirmed the amorphous nature of the as-deposited films. Post-sulfurization, both types of films exhibited crystalline hexagonal MoS<sub>2</sub> phases, with the sulfurized Mo showing a polycrystalline nature with a (100) orientation and sulfurized MoS<sub>2</sub> displaying a (00L) preferred orientation. The X-ray photoelectron spectroscopy results supported a Mo:S ratio of 1:2 on the surface of the films obtained using the MoS<sub>2</sub> precursor films, confirming the stoichiometry obtained by means of energy dispersive X-ray spectroscopy. Scanning electron microscopy and atomic force microscopy images revealed micrometer-sized clusters potentially formed during rapid cooling post-sulfurization, with an increased average roughness. These results open the way for the further exploration of wrinkled MoS<sub>2</sub> thin films in advanced energy storage technologies.

**Keywords:** wrinkled MoS<sub>2</sub>; TMDs; thin films; magnetron sputtering; sulfurization



**Citation:** Mihai, C.; Simandan, I.-D.; Sava, F.; Buruiana, A.-T.; Bocirnea, A.E.; Tite, T.; Zaki, M.Y.; Velea, A. Synthesis of Wrinkled MoS<sub>2</sub> Thin Films Using a Two-Step Method Consisting of Magnetron Sputtering and Sulfurization in a Confined Space. *Sustainability* **2024**, *16*, 3819. <https://doi.org/10.3390/su16093819>

Academic Editor: Vito Rizzi

Received: 6 April 2024

Revised: 25 April 2024

Accepted: 29 April 2024

Published: 1 May 2024



**Copyright:** © 2024 by the authors. Licensee MDPI, Basel, Switzerland. This article is an open access article distributed under the terms and conditions of the Creative Commons Attribution (CC BY) license (<https://creativecommons.org/licenses/by/4.0/>).

## 1. Introduction

The rapid expansion of the electric vehicle and portable electronic device markets has escalated the demand for energy storage systems with a high energy density and a substantial power output [1,2]. In response, significant research efforts have been directed towards developing efficient energy storage devices, such as batteries and supercapacitors [3,4]. Among various materials, MoS<sub>2</sub>, a two-dimensional layered inorganic material, has emerged as a good candidate for energy conversion and storage applications due to its adjustable bandgap and unique electronic and physicochemical properties [5–9]. In particular, the layered structure of MoS<sub>2</sub> promotes efficient electron and ion transport, desirable for high-performance energy storage devices, and its bandgap manipulation enhances electrical conductivity and electrochemical properties. These characteristics are highly beneficial in increasing energy density, improving charge–discharge rates, enhancing

cycle stability in battery technology, and boosting capacitance and energy efficiency in supercapacitors [10–14]. Molybdenum disulfide has also been widely used as a solid lubricant [15]. Its combination with other tribological materials such as DLC [16] and high-wear-resistance  $Ti_3C_2T_x$  was recently discussed [17–19].

Given the growing demand for environmentally friendly and cost-effective energy storage systems,  $MoS_2$  integration into these systems is a significant advance towards achieving energy sustainability and efficiency. The unique structure of layered materials, including  $MoS_2$ , offers advantages in energy storage applications due to their high surface area-to-volume ratio and observable characteristics within a few atomic layers [20,21]. However, challenges such as poor cycle stability due to structural deterioration during charge/discharge cycles have prompted research into nanostructuring  $MoS_2$  to enhance ion kinetics, thus improving overall battery performance [13,22]. The development of such nanostructured  $MoS_2$  anodes is crucial for overcoming the limitations of bulk  $MoS_2$ , particularly in terms of cycling stability and rate capability, thereby making it more viable for practical applications in advanced batteries and supercapacitors [23].

Regarding material synthesis, magnetron sputtering is a superior technique for depositing thin films, offering uniformity, smoothness, and precise control over layer thickness, essential for creating high-quality  $MoS_2$  thin films [24,25]. However, the reliance of CVD on chemical precursors can pose more sustainability challenges in terms of chemical handling, safety, and disposal. Moreover, magnetron sputtering is more material-efficient, which is beneficial for sustainability. Additionally, it can easily be used for doping to improve the properties of  $MoS_2$  coatings [26]. Wu et al. [27] demonstrated the potential of this method to obtain thin  $MoS_2$  films through the sequential deposition of Mo layers and controlled sulfurization [28,29]. During the sulfurization, there is competition between Mo oxide segregation leading to the formation of small clusters and the sulfurization reaction leading to planar  $MoS_2$ . The most common sulfurization methods involve conducting annealing in  $H_2S$ - or  $S_2$ -containing atmospheres. However,  $H_2S$  is a toxic gas, while the contamination of the medium becomes an important issue when the annealing is conducted in a  $S_2$  environment due to the formation of  $SO_2$  [30,31].

In this study,  $MoS_2$  thin films were synthesized in a two-step process consisting of magnetron sputtering deposition of two types of precursors, namely Mo and  $MoS_2$  layers, followed by sulfurization in a graphite box. This novel approach significantly reduces the S quantity up to ten times during sulfurization due to the confined space and represents an important advancement in the controlled synthesis of nanostructured  $MoS_2$  thin films on Si/ $SiO_2$  substrates. It also contributes to avoiding the formation of toxic gases such as  $SO_2$  or the necessity of using  $H_2S$  for sulfurization, aligning with the need for efficient and sustainable energy storage solutions.

## 2. Materials and Methods

The  $MoS_2$  films were obtained using a two-step process involving the deposition of a precursor thin film of either Mo or  $MoS_2$ , followed by sulfurization in a confined space. The method is depicted in Figure 1. In the first step, molybdenum and molybdenum disulfide precursor thin films were deposited using a custom-built magnetron sputtering system [32]. Commercial Mo and  $MoS_2$  targets (Mateck, Jülich, Germany, 99.9% purity, 5 cm in diameter and 3 mm thickness) were used. The process was initiated in a vacuum of  $6.5 \times 10^{-6}$  Torr. Argon was introduced at a constant flow of 30 sccm and the chamber pressure increased to  $6 \times 10^{-3}$  Torr, which was kept constant during the deposition. The Mo target received a power of 26 W from a T&C Power Conversion AG 0313 RF source (Rochester, NY, USA) for 1886 s, while the  $MoS_2$  target received 18 W for 1785 s from the same RF source. The used Si substrates with a 90 nm  $SiO_2$  layer were continuously rotated during deposition for thickness uniformity.

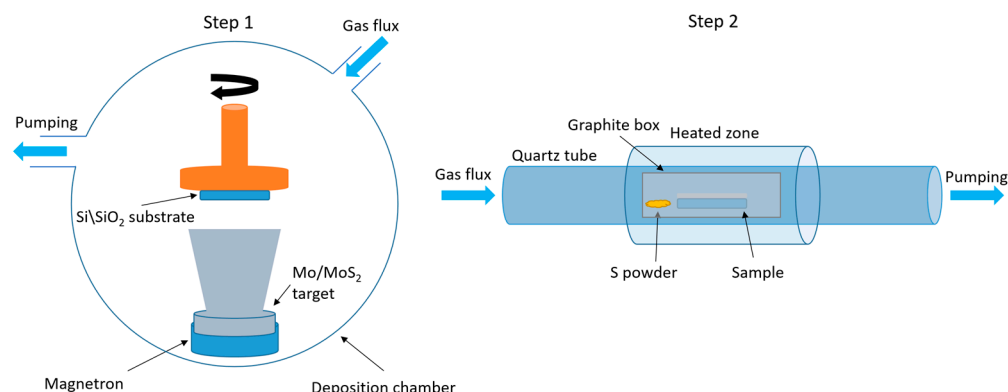


**Figure 1.** The two-step process for the deposition of MoS<sub>2</sub> thin films. Step 1 consists of magnetron sputtering deposition of Mo and MoS<sub>2</sub> precursor films, while in step 2, the obtained films are sulfurized in a graphite box.

Post-deposition, in the second step, the Mo and MoS<sub>2</sub> films underwent a sulfurization process. Enclosed in a graphite box with 0.025 g of sulfur, the samples were placed in an MTI GSL 1600X (MTI Corporation, Richmond, CA, USA) quartz tube furnace. The system was vacuumed and pressurized with argon to 0.03 MPa. The thermal treatment was performed at 800 °C for 45 min, with a ramp and cooling rate of 10 °C/min.

The samples were subjected to detailed morphological and elemental analysis using a Zeiss Gemini 500 Field Emission Scanning Electron Microscope (SEM) equipped with a Bruker energy dispersive X-ray (EDX) spectrometer (Bruker, Billerica, MA, USA). The crystalline structures of the samples were investigated using X-ray diffraction (XRD) and grazing incidence X-ray diffraction (GIXRD). This analysis was performed using a Rigaku SmartLab diffractometer (Rigaku Corporation, Tokyo, Japan), set in a parallel beam arrangement, provided with copper K $\alpha$  radiation ( $\lambda = 1.54187 \text{ \AA}$ ) and a HyPix-3000 2D Hybrid Pixel Array Detector (Rigaku Corporation, Tokyo, Japan) used in 0D and 1D modes. The diffractograms were recorded from 5° to 65° (2 $\theta$ ) with a step size of 0.04° and the measuring time per step was 2 s for GIXRD and 40 s for XRD ( $\theta$ -2 $\theta$  Bragg–Brentano geometry). The incident angle was precisely adjusted to enhance diffraction conditions for GIXRD. The background of the diffractograms was subtracted. X-ray reflectometry (XRR) patterns were captured using the same equipment. The thickness and mass density of the samples were accurately determined using Leptos software (version 4.01 from Bruker), which allows for the alignment of simulated XRR curves with the experimentally obtained data. Additional micro-Raman (m-Raman) structural examination was carried out with a LabRam HR Evolution spectrometer (Horiba Jobin Yvon, Palaiseau, France) equipped with a Sincerity OE detector. The measurements were performed by focusing a He-Ne laser ( $\lambda = 633 \text{ nm}$ ) on the surface of the samples in backscattering geometry with an Olympus MPlanN 100 $\times$ /0.90 numerical aperture using a diffraction grating of 1800 lines/mm. The spectra were recorded in the range 50–600 cm<sup>-1</sup> for an acquisition time of 10 s and 25 accumulations with a neutral density filter of 50% and 5% of the maximum laser power for a confocal hole of 100  $\mu\text{m}$  for the target and thin films, respectively. This corresponds to a laser power of 750 and 75  $\mu\text{W}$ , respectively. The maximum visible spot that excites the laser corresponded to the Airy spot was  $\sim 0.85 \mu\text{m}$ . Atomic force microscopy (AFM) imaging was performed using an NT-MDT Aura Ntegra Prima atomic force microscope (Amsterdam, Netherlands) in a non-contact mode. The surface of the films was characterized by means of X-ray photoelectron spectroscopy (XPS) using a monochromatized Al K $\alpha$  source at 1486.6 eV and a power of 144 W (12 kV  $\times$  12 mA), employing a Kratos Axis Ultra spectrometer (Kratos Analytical Ltd., Manchester, UK). The analyzer was operated in the fixed analyzer transmission (FAT) mode, and the high-resolution spectra were acquired at 40 eV pass energy and 0.05 eV energy step. The analysis of the S 2p and Mo 3d doublets was performed after spectral deconvolution with Voigt profiles including two Lorentzian

components. Both the spectral deconvolution extraction of the Shirley background and the data analysis were performed using IGOR Pro 9 software.

### 3. Results

#### 3.1. X-ray Reflectometry (XRR) Measurements

The XRR diagrams and the corresponding fitted curves for the Mo and MoS<sub>2</sub> precursor thin films are depicted in Figure 2(a1,a2). We determined the thickness of the Mo precursor layer to be 14.4 nm and its average mass density to be 8.0 g/cm<sup>3</sup>, compared to 10.28 g/cm<sup>3</sup> [33] for a bulk Mo monocrystal. For the MoS<sub>2</sub> precursor layer, the values obtained were 18.0 nm for the thickness and an average mass density of 4.3 g/cm<sup>3</sup>, against 5.06 g/cm<sup>3</sup> [33] for a bulk MoS<sub>2</sub> monocrystal. The observed variations in mass density of the Mo and MoS<sub>2</sub> thin films, as compared to their bulk monocrystal counterparts, can be attributed to structural differences, the presence of defects or voids, surface roughness, and deviations in film composition.

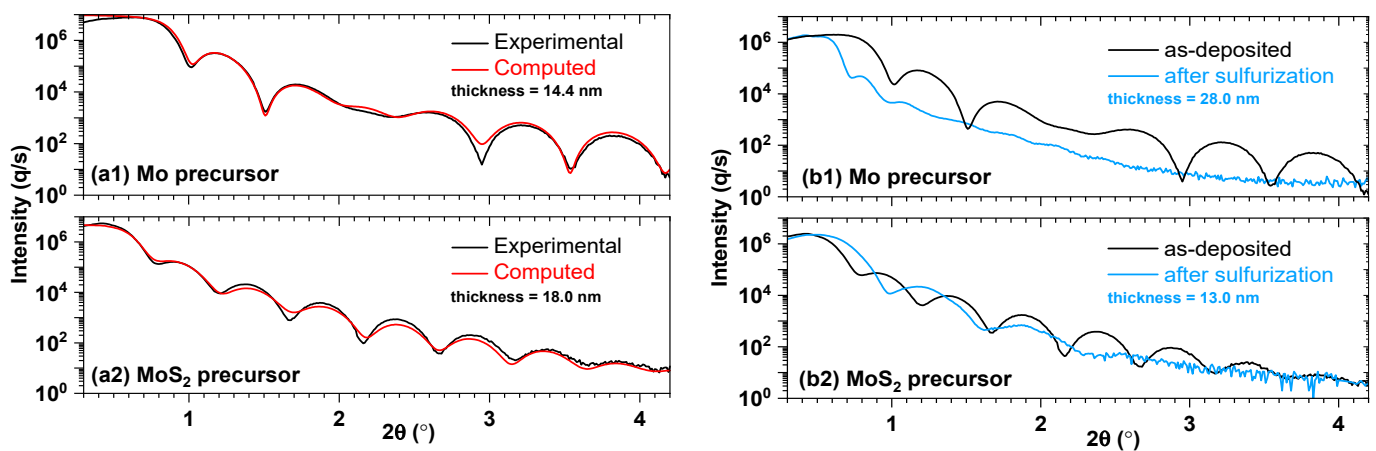


**Figure 2.** XRR diagrams of the (a1,a2) as-deposited (black) and the corresponding fitted XRR curves (red), and (b1,b2) sulfurized (blue) Mo and MoS<sub>2</sub> precursor thin films.

The XRR diagrams for the sulfurized Mo and MoS<sub>2</sub> thin films are shown in Figure 2(b1,b2). The thickness of the Mo film is 28 nm. Theoretically, a thickness of approximately 55 nm was expected if the as-deposited Mo film would have been entirely sulfurized. In contrast, the sulfurized MoS<sub>2</sub> layer showed a uniform thickness of 13 nm, compared with a theoretical expectation of around 18 nm. The observed discrepancy in thickness and structure between the theoretical expectations and the experimental results can be attributed to several factors. In the case of the Mo layer, the formation of a thick 28 nm layer indicates a significant reaction during sulfurization, leading to an expanded or altered structure. This might be due to the diffusion of sulfur into the Mo layer or the formation of an additional MoS<sub>2</sub> layer on top of the original Mo. For the sulfurized MoS<sub>2</sub> layer, the reduction in thickness from the expected value might be due to the loss of material and an increase in density during sulfurization. The uniformity of this layer suggests a more controlled and consistent reaction compared to the Mo layer.

#### 3.2. X-ray Diffraction

The X-ray diffraction diagrams at grazing incidence for the Mo (Figure 3(a1)) and MoS<sub>2</sub> (Figure 3(b1)) precursor thin films were obtained at an incidence angle of 0.3°. The broad peaks observed in both diagrams suggest that each of the layers possesses an amorphous, disordered structure. This is in contrast with the distinct crystalline peaks of the substrate, which are clearly discernible. The amorphous nature indicated by the GIXRD analysis complements the findings from the XRR measurements, explaining the lower density as compared to their crystalline monocrystal forms.

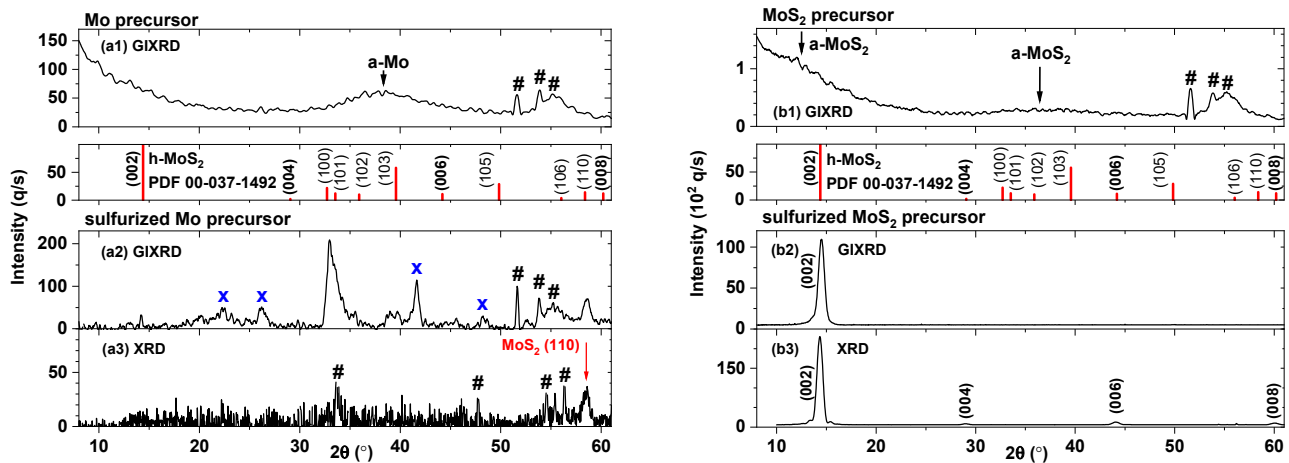


**Figure 3.** GIXRD diagrams for (a1,b1) as-deposited and (a2,b2) sulfurized Mo and MoS<sub>2</sub> precursor thin films, and (a3,b3) the XRD diagrams of the sulfurized samples. The broad peaks denoted as a-Mo and a-MoS<sub>2</sub> are from amorphous phases. The diffraction peaks marked with ‘#’ and ‘x’ markers are from the silicon substrate and from an unidentified crystalline phase, respectively. The data from the PDF 00-037-1492 of h-MoS<sub>2</sub> are also presented.

The GIXRD diagrams, performed with the detector in 0D mode, and XRD diagrams, obtained using Bragg–Brentano geometry with the detector in 1D mode, for sulfurized Mo and MoS<sub>2</sub> precursors are displayed in Figure 3(a2,b2), and (a3,b3), respectively. In both cases, the data confirm the successful synthesis of the hexagonal MoS<sub>2</sub> (h-MoS<sub>2</sub>) phase according to PDF 00-037-1492, highlighting the effectiveness of the sulfurization process. Sulfurized Mo exhibits a polycrystalline structure with a preferential (100) orientation. Most of the MoS<sub>2</sub> crystallites have layers in the plane (002) that are not parallel to the substrate but perpendicular.

On the other hand, the sulfurized MoS<sub>2</sub> precursor shows a preferential (00L) orientation. In this case, the MoS<sub>2</sub> layers are parallel to the substrate. The polycrystalline nature of the sulfurized Mo film and the (100) preferential orientation suggest a distinct structural rearrangement post-sulfurization. This perpendicular arrangement might generate an anisotropic electronic transport mechanism that could influence the charge carrier mobility and mechanical stress distribution within the layer, potentially impacting its application in electronic devices, but beneficial for applications such as catalysis and energy storage. In contrast, the preferential (00L) orientation, parallel to the substrate, of the MoS<sub>2</sub> crystallites in sulfurized MoS<sub>2</sub>, indicative of a layered structure, is beneficial for applications requiring a high surface area, as in electronic devices, where the directionality of electronic and ionic transport plays an important role in device performance.

### 3.3. Micro Raman Spectroscopy

The hexagonal MoS<sub>2</sub> exhibits four Raman peaks: E<sub>2g</sub><sup>2</sup> at 32 cm<sup>-1</sup>, which requires high spectral resolution Raman spectrometers for detection and corresponds to the interlayer vibration within MoS<sub>2</sub>; E<sub>1g</sub> at 286 cm<sup>-1</sup> (forbidden in backscattering geometry on surfaces perpendicular to the c-axis); E<sub>2g</sub><sup>1</sup> at 381 cm<sup>-1</sup>; and A<sub>1g</sub> at 408 cm<sup>-1</sup> [34]. Other peaks in the m-Raman spectra arise due to the resonance phenomenon between the excitation laser radiation (633 nm) and the MoS<sub>2</sub> band gap. This resonance, alongside the coupling between electronic transitions (correlated with excitonic states) and phonon modes, significantly amplifies the second- or higher-order Raman scattering.

The m-Raman spectra of the as-deposited Mo and MoS<sub>2</sub> thin films did not show any Raman peaks, indicating that they are completely amorphous, as confirmed by the X-ray diffraction diagrams (Figure 3(a1,b1)).

The m-Raman spectra of the sulfurized Mo sample (Figure 4a, blue curve) and sulfurized MoS<sub>2</sub> sample (Figure 4a, red curve) confirm that sulfurization led to the formation

of the hexagonal crystalline MoS<sub>2</sub> phase. The red curve is similar to the spectrum of the solid MoS<sub>2</sub> sputtering target (Figure 4b). The A<sub>1g</sub> peak shows a shoulder at 402 cm<sup>-1</sup>; consequently, the frequency difference ( $\delta$ ) of the two Raman modes, E<sub>2g</sub><sup>1</sup> and A<sub>1g</sub>, decreases from 28 cm<sup>-1</sup> to 22 cm<sup>-1</sup>. This means that on average, there are two categories of crystallites thicknesses in each sample. The majority category is represented by thick crystallites containing more than four MoS<sub>2</sub> layers, while the second category is formed by three MoS<sub>2</sub> layers [35].

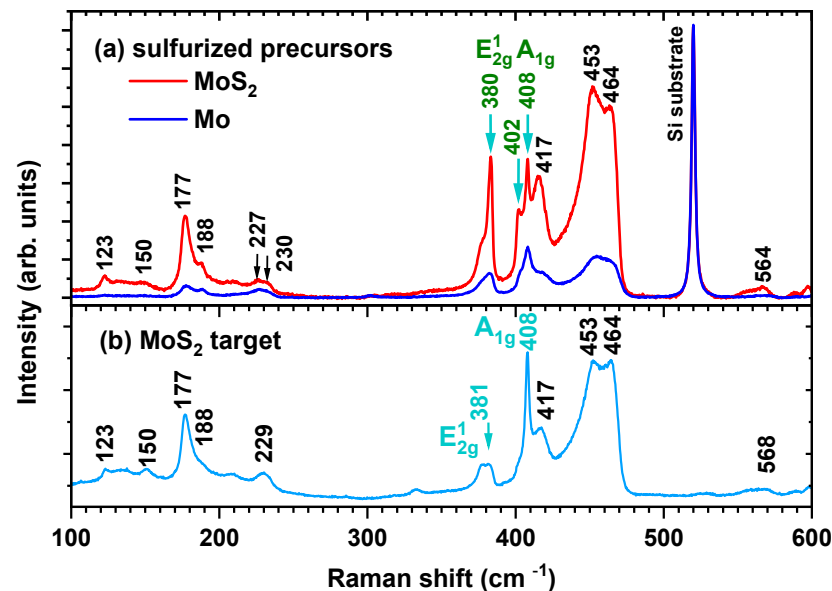


**Figure 4.** Raman spectra at an excitation wavelength of 633 nm for the (a) sulfurized Mo (blue curve) and MoS<sub>2</sub> (red curve) precursor thin films and (b) MoS<sub>2</sub> target used in magnetron sputtering (as provided by the manufacturer).

Due to the resonance conditions, second-order Raman bands at 123 cm<sup>-1</sup>, 150 cm<sup>-1</sup>, 177 cm<sup>-1</sup>, 188 cm<sup>-1</sup>, 227 cm<sup>-1</sup>, 230 cm<sup>-1</sup>, 417 cm<sup>-1</sup>, 453 cm<sup>-1</sup>, 464 cm<sup>-1</sup>, and 564 cm<sup>-1</sup> [36–38] are also visible. The work of Livneh et al. [37] facilitates the symmetry assignments of these peaks:

- A<sub>1g</sub>(Γ)—E<sub>1g</sub>(Γ) for the peak at 123 cm<sup>-1</sup>;
- E<sub>2g</sub><sup>1</sup>(K<sub>2</sub>)—LA'(K) for the peak at 150 cm<sup>-1</sup>, where LA'(K) is the longitudinal quasi-acoustic optical phonon in K point of the hexagonal Brillouin zone. A different process involves the creation of one phonon while absorbing another;
- A<sub>1g</sub>(M)—LA(M) for the peak at 177 cm<sup>-1</sup>, where LA(M) is the longitudinal acoustic phonon in M point of the hexagonal Brillouin zone. The asymmetric line shape arising from phonon dispersion of LA mode demonstrates a concave dispersion towards the M point [39]. Notably, the characteristic MoS<sub>2</sub> modes, A<sub>1g</sub> and E<sub>2g</sub><sup>1</sup>, show no dispersion in the Γ-M direction;
- E<sub>2g</sub><sup>1</sup>(M<sub>2</sub>)—ZA'(M) for the peak at 188 cm<sup>-1</sup>, which exhibits an exponential temperature dependence, detectable even at liquid nitrogen temperatures [36];
- A degenerate van Hove singularity (vHs) is located between the K and M points for the peak at 227 cm<sup>-1</sup>, while its intensity is proportional to the disorder degree [34]. The diminished intensity of this peak in the sulfurized MoS<sub>2</sub> film, compared to the sulfurized Mo film, can be attributed to the higher crystalline quality and reduced disorder and defects in the MoS<sub>2</sub> film post-sulfurization;
- LA'(M) for the peak at 230 cm<sup>-1</sup>;
- A<sub>1g</sub>(M) for the peak at 417 cm<sup>-1</sup> [36];
- The most pronounced band among the second-order Raman peaks, at 453 cm<sup>-1</sup>, is attributed to the overlap of the vHs from two phonon branches located between

the K and M points, each resonating near the frequency of  $227\text{ cm}^{-1}$ . The peak at  $453\text{ cm}^{-1}$  exhibits significantly greater intensity in the sulfurized  $\text{MoS}_2$  film. This could be due to increased resonance effects between the laser excitation and the  $\text{MoS}_2$  band gap. Additionally, the intensity variations of this band inversely correlate with defect concentrations [38,40] (for the first-order peak, at  $227\text{ cm}^{-1}$ , the intensity is proportional with defect concentrations). Accordingly, the sulfurized  $\text{MoS}_2$  film has a relatively low defect density within the  $\text{MoS}_2$  layers, enhancing the resonance Raman effect;

- $\text{LA}'(\text{M}) + \text{LA}(\text{M})$  for the peak at  $464\text{ cm}^{-1}$ ;
- $\text{A}_{1g}(\text{M}) + \text{TA}'(\text{M})$  for the peak at  $564\text{ cm}^{-1}$ , where  $\text{TA}'(\text{M})$  is a transversal quasi-acoustic optical phonon in M point of the hexagonal Brillouin zone.

### 3.4. Scanning Electron Microscopy

The scanning electron microscopy images obtained on sulfurized Mo films (Figure 5a) indicate elongated formations ranging from 1 to 7 microns in length on the surface of the samples, as compared with the as-deposited samples, which display a dense, compact surface with minimal roughness for both Mo and  $\text{MoS}_2$  thin films. The sulfurized  $\text{MoS}_2$  sample (Figure 5b) exhibits a less uniform surface, composed of small nanometric clusters from 1 to 10 microns in length. These formations are attributed to a phenomenon known as ‘surface wrinkling’, occurring when rapid cooling from  $800\text{ }^\circ\text{C}$  to room temperature takes place. The ‘surface wrinkling’ [41] phenomenon observed in both samples is a significant aspect of the cooling process following high-temperature treatments. This feature indicates the presence of mechanical stresses and structural rearrangements occurring during rapid cooling.

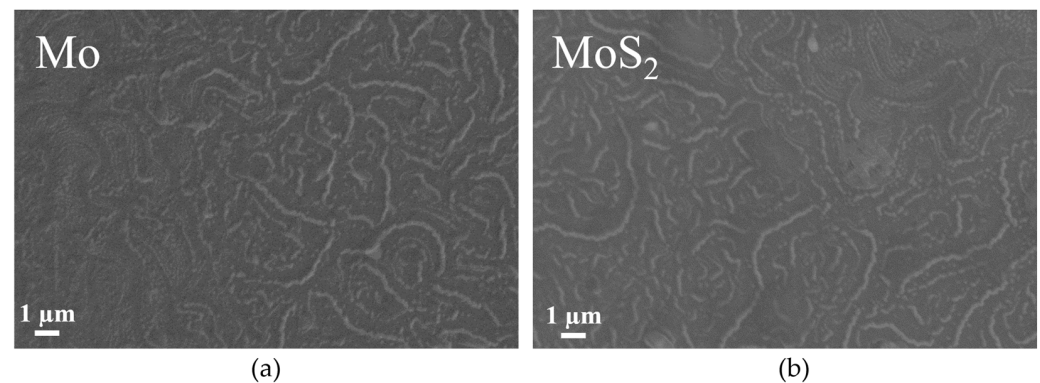


**Figure 5.** SEM images of the sulfurized samples: (a) Mo and (b)  $\text{MoS}_2$ .

Using EDX, we measured the composition of the sulfurized Mo and  $\text{MoS}_2$  thin films, and the results are shown in Table 1. For the sulfurized Mo sample, the composition is  $\text{Mo}_{40}\text{S}_{60}$ , while for the sulfurized  $\text{MoS}_2$  sample, it is  $\text{Mo}_{34}\text{S}_{66}$ . The results show a substantial incorporation of sulfur in the Mo film, indicating a successful sulfurization process. However, the Mo-rich nature of this composition compared to the ideal Mo:S ratio of 1:2 (or  $\text{Mo}_{33.33}\text{S}_{66.67}$  in atomic percentages) suggests the incomplete incorporation of sulfur. This could be due to various factors such as the initial thickness of the Mo layer, the sulfurization temperature, or the duration of the sulfurization process. The sulfurized  $\text{MoS}_2$  ( $\text{Mo}_{34}\text{S}_{66}$ ) is very close to the ideal stoichiometry, indicating that the sulfurization process was highly effective.

**Table 1.** Composition of sulfurized Mo and  $\text{MoS}_2$  thin films after sulfurization.

Precursor	Composition
Mo	$\text{Mo}_{40}\text{S}_{60}$
$\text{MoS}_2$	$\text{Mo}_{34}\text{S}_{66}$

### 3.5. Atomic Force Microscopy

Figure 6 shows the AFM image obtained for the sulfurized MoS<sub>2</sub> sample, where elongated formations are visible on the surface, corroborating the observations made in the SEM analysis. Utilizing a cantilever equipped with a sharp tip to probe the surface, we determined the surface roughness to be significantly high, measured at 20 nm. This measurement reveals an intriguing aspect of the material morphology, namely that the surface roughness surpasses the film thickness, which was previously estimated to be 13 nm post-sulfurization. Typically, a roughness greater than the film thickness suggests a highly textured surface with pronounced topographical features that extend beyond the general plane of the film. Such a condition could impact the film's physical properties and its interaction with the environment, potentially affecting applications where surface area and texture play important roles, such as in catalysis, sensing, or energy storage devices. The pronounced roughness indicates a complex surface morphology that may influence the electronic, mechanical, and chemical behavior of the MoS<sub>2</sub> thin film.

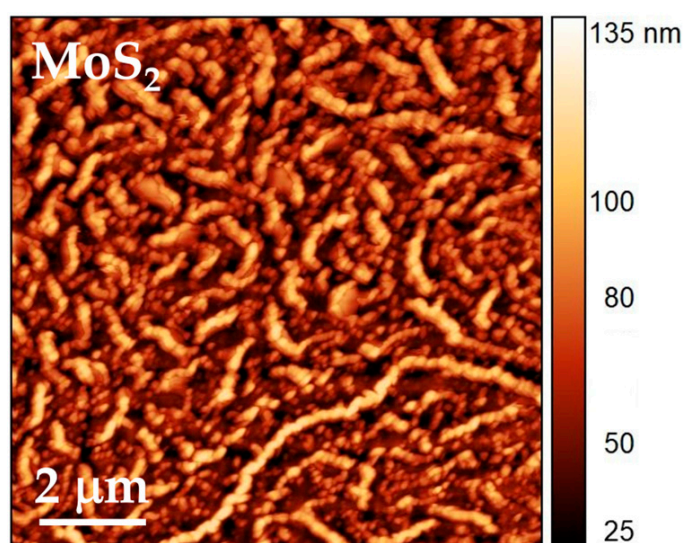
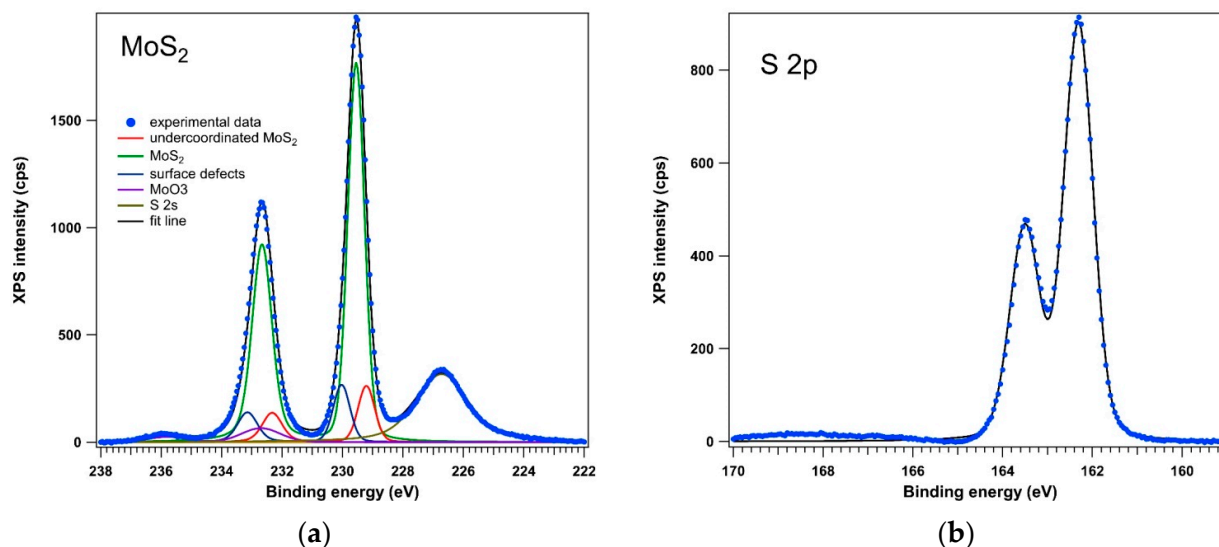


Figure 6. AFM image of the sulfurized MoS<sub>2</sub> sample.

### 3.6. X-ray Photoelectron Spectroscopy

Since the thin film obtained from the MoS<sub>2</sub> target and subsequently thermally treated in a sulfur atmosphere proved to be of high quality and homogeneous when characterized by “bulk techniques”, the quality of the surface and its stability were also checked by means of photoemission spectroscopy. The results are presented in Figure 7. The Mo 3d spectrum was deconvoluted into four components for Mo and a singlet corresponding to S 2s at a binding energy of 226.7 eV. The component at higher binding energies of 232.7 eV is attributed to MoO<sub>3</sub>. The other three components at binding energies of 229.2 eV, 229.5 eV, and 230 eV are associated with S-deficient MoS<sub>2</sub>, bulk MoS<sub>2</sub>, and surface MoS<sub>2</sub>, respectively. The S 2p spectrum was deconvoluted into a single component attributed to S<sup>2-</sup> at a binding energy of 162.3 eV, showing that all sulfur participates in Mo-S bonds and that there is no unreacted S-S.

Considering that the three main contributions of Mo 3d are related to S, the Mo:S ratio on the analyzed surface is approximately 1:2, as indicated by the ratio of the integral amplitudes corrected for photoionization cross-section, a result also confirmed by the identification of the thin film composition through EDX.



**Figure 7.** Experimental XPS spectra of (a) Mo 3d and (b) S 2p along with the components extracted from deconvolutions.

#### 4. Discussion

The two-step process employed herein, utilizing magnetron sputtering and a confined space for sulfurization [42], exemplifies a significant advancement towards sustainability. This method, characterized by a small energy footprint and a high material efficiency demonstrates an energy- and resource-conserving approach to material synthesis. By optimizing the annealing conditions, including the innovative use of a graphite box for sulfurization, this study not only ensures the precise control of the chemical environment but also minimizes the potential waste and environmental impact. Moreover, this approach eliminates the necessity of using toxic  $H_2S$  gas. Such a methodology is important in advancing the  $MoS_2$  material synthesis towards more sustainable practices.

Supercapacitors and batteries, characterized by their compact size, low thickness, and mechanical robustness, are essential for integration into flexible electronics. Utilizing materials with wrinkled structures as electrodes can fulfill these requirements. The increased specific surface area and minimized height of wrinkled films enhance their synergy with electrochemically active materials, boosting performance. Moreover, such supercapacitors demonstrate stable operation under mechanical stress due to the added flexibility provided by the wrinkles. Additionally, lithium and lithium–sulfur batteries significantly benefit from the unique properties of wrinkled electrode materials, including high stretchability and specific surface area, thus enhancing their performance.

Compared to traditional capacitors, electrodes prepared from thin films with wrinkled structures demonstrate superior qualities in supercapacitors [43–49]. Wrinkles notably reduce electrode resistance, a fundamental requirement for high-performing supercapacitors. Moreover, integrating supercapacitors into wearable electronics demands resilience under mechanical strains [50], making the development of wrinkled structures essential. Additionally, wrinkled structures serve to anchor transition metal oxides or metal nanoparticles onto thin films, enhancing specific capacitance. Thus, these thin, flexible, and eco-friendly supercapacitors hold great potential for energy storage and supply applications, leveraging the unique advantages of wrinkled electrode architectures.

High-energy lithium-ion and lithium–sulfur (Li-S) batteries are at the forefront of next-generation energy storage technologies, despite facing certain challenges. The quest for a high specific capacity has led to increased interest in Li-alloy-based batteries [51,52]. In Li-S batteries, the generation of lithium polysulfides during cycling reduces sulfur utilization and diminishes the amount of active material, limiting battery performance [53]. The use of wrinkled sheets to encapsulate sulfur leverages their ample nanopores to increase specific surface area and polysulfide absorption. The wrinkles act as physical barriers, mitigating

polysulfide shuttle effects and significantly boosting cyclability. Batteries incorporating wrinkled thin films, serving both as active holders and flexible supporters, emerge as viable candidates for future energy storage solutions, capitalizing on the unique mechanical and chemical properties of wrinkled structures to overcome longstanding challenges.

## 5. Conclusions

This study successfully produced wrinkled MoS<sub>2</sub> thin films using a novel sustainable two-step approach, namely the sputtering of a precursor Mo or MoS<sub>2</sub> film followed by sulfurization in a graphite box. Better results were obtained when MoS<sub>2</sub> precursor thin films are used, suggesting that the existence of S in the film increases the efficiency of the sulfurization process. These thin films were characterized as being textured using X-ray diffraction, and the MoS<sub>2</sub> crystallites grew with their (00L) planes preferentially oriented parallel to the substrate surface. Micro-Raman spectroscopy confirmed the hexagonal structure and revealed a relatively low defect density within the layer. Additionally, surface morphology assessments via SEM and AFM also illustrated varied textures, with notable surface wrinkling resulting from thermal processing dynamics. Chemical composition examinations through XPS confirmed a Mo:S ratio near 1:2, suggestive of MoS<sub>2</sub> synthesis. The wrinkles obtained on the film surfaces post-sulfurization pave the way for tailored application in energy storage, further highlighting the role of advanced materials in the development of sustainable technological solutions.

**Author Contributions:** Conceptualization, C.M. and A.V.; methodology, C.M. and A.V.; formal analysis, F.S., I.-D.S., A.-T.B., A.E.B., T.T. and M.Y.Z.; investigation, F.S., I.-D.S., A.-T.B., A.E.B., T.T. and M.Y.Z.; resources, I.-D.S. and A.V.; data curation, C.M., F.S. and I.-D.S.; writing—original draft preparation, C.M., I.-D.S. and A.V.; writing—review and editing, C.M., I.-D.S., F.S., A.-T.B., A.E.B., T.T., M.Y.Z. and A.V.; visualization, C.M., I.-D.S. and F.S.; supervision, A.V.; project administration, I.-D.S.; funding acquisition, I.-D.S. All authors have read and agreed to the published version of the manuscript.

**Funding:** This work is funded by the Core Program of the National Institute of Materials Physics, granted by the Romanian Ministry of Research, Innovation and Digitization through the Project PC3-PN23080303.

**Institutional Review Board Statement:** Not applicable.

**Informed Consent Statement:** Not applicable.

**Data Availability Statement:** The data presented in this study are available in this article.

**Conflicts of Interest:** The authors declare no conflicts of interest.

## References

1. Larcher, D.; Tarascon, J.-M. Towards Greener and More Sustainable Batteries for Electrical Energy Storage. *Nat. Chem.* **2015**, *7*, 19–29. [[CrossRef](#)] [[PubMed](#)]
2. Repp, S.; Harputlu, E.; Gurgen, S.; Castellano, M.; Kremer, N.; Pompe, N.; Wörner, J.; Hoffmann, A.; Thomann, R.; Emen, F.M.; et al. Synergetic Effects of Fe<sup>3+</sup> Doped Spinel Li<sub>4</sub>Ti<sub>5</sub>O<sub>12</sub> Nanoparticles on Reduced Graphene Oxide for High Surface Electrode Hybrid Supercapacitors. *Nanoscale* **2018**, *10*, 1877–1884. [[CrossRef](#)] [[PubMed](#)]
3. Armand, M.; Tarascon, J.-M. Building Better Batteries. *Nature* **2008**, *451*, 652–657. [[CrossRef](#)] [[PubMed](#)]
4. Wang, K.-B.; Xun, Q.; Zhang, Q. Recent Progress in Metal–Organic Frameworks as Active Materials for Supercapacitors. *EnergyChem* **2020**, *2*, 100025. [[CrossRef](#)]
5. Jeong, G.H.; Sasikala, S.P.; Yun, T.; Lee, G.Y.; Lee, W.J.; Kim, S.O. Nanoscale Assembly of 2D Materials for Energy and Environmental Applications. *Adv. Mater.* **2020**, *32*, 1907006. [[CrossRef](#)] [[PubMed](#)]
6. Cao, X.; Tan, C.; Zhang, X.; Zhao, W.; Zhang, H. Solution-Processed Two-Dimensional Metal Dichalcogenide-Based Nanomaterials for Energy Storage and Conversion. *Adv. Mater.* **2016**, *28*, 6167–6196. [[CrossRef](#)] [[PubMed](#)]
7. Yu, X.; Hu, H.; Wang, Y.; Chen, H.; Lou, X.W.D. Ultrathin MoS<sub>2</sub> Nanosheets Supported on N-doped Carbon Nanoboxes with Enhanced Lithium Storage and Electrocatalytic Properties. *Angew. Chem.* **2015**, *54*, 7395–7398. [[CrossRef](#)] [[PubMed](#)]
8. Kam, K.K.; Parkinson, B.A. Detailed Photocurrent Spectroscopy of the Semiconducting Group VIB Transition Metal Dichalcogenides. *J. Phys. Chem.* **1982**, *86*, 463–467. [[CrossRef](#)]

9. Mak, K.F.; Lee, C.; Hone, J.; Shan, J.; Heinz, T.F. Atomically Thin MoS<sub>2</sub>: A New Direct-Gap Semiconductor. *Phys. Rev. Lett.* **2010**, *105*, 136805. [[CrossRef](#)]
10. Tan, C.; Zhang, H. Two-Dimensional Transition Metal Dichalcogenide Nanosheet-Based Composites. *Chem. Soc. Rev.* **2015**, *44*, 2713–2731. [[CrossRef](#)]
11. Zhu, C.; Mu, X.; van Aken, P.A.; Yu, Y.; Maier, J. Single-Layered Ultrasmall Nanoplates of MoS<sub>2</sub> Embedded in Carbon Nanofibers with Excellent Electrochemical Performance for Lithium and Sodium Storage. *Angew. Chem.* **2014**, *53*, 2152–2156. [[CrossRef](#)]
12. Zhu, C.; Mu, X.; Van Aken, P.A.; Maier, J.; Yu, Y. Fast Li Storage in MoS<sub>2</sub>-Graphene-Carbon Nanotube Nanocomposites: Advantageous Functional Integration of 0D, 1D, and 2D Nanostructures. *Adv. Energy Mater.* **2015**, *5*, 1401170. [[CrossRef](#)]
13. Liu, C.; Li, F.; Ma, L.; Cheng, H. Advanced Materials for Energy Storage. *Adv. Mater.* **2010**, *22*, E28–E62. [[CrossRef](#)] [[PubMed](#)]
14. Joseph, N.; Shafi, P.M.; Bose, A.C. Recent Advances in 2D-MoS<sub>2</sub> and Its Composite Nanostructures for Supercapacitor Electrode Application. *Energy Fuels* **2020**, *34*, 6558–6597. [[CrossRef](#)]
15. Gradt, T.; Schneider, T. Tribological Performance of MoS<sub>2</sub> Coatings in Various Environments. *Lubricants* **2016**, *4*, 32. [[CrossRef](#)]
16. Ould, C.; Tite, T.; Héau, C.; Loir, A.-S.; Donnet, C.; Garrelie, F. Tribological Behavior of DLC Film Models in Base Oils: Analysis of Influence of Sp<sup>3</sup>/Sp<sup>2</sup> Ratio and Hydrogen Content. *Tribol. Int.* **2024**, *194*, 109446. [[CrossRef](#)]
17. Wang, C.; Hausberger, A.; Nothdurft, P.; Lackner, J.M.; Schwarz, T. The Potential of Tribological Application of DLC/MoS<sub>2</sub> Coated Sealing Materials. *Coatings* **2018**, *8*, 267. [[CrossRef](#)]
18. Tremmel, S.; Luo, X.; Rothhammer, B.; Seynstahl, A.; Wang, B.; Rosenkranz, A.; Marian, M.; Zhu, L. Evaluation of DLC, MoS<sub>2</sub>, and Ti<sub>3</sub>C<sub>2</sub>T<sub>x</sub> Thin Films for Triboelectric Nanogenerators. *Nano Energy* **2022**, *97*, 107185. [[CrossRef](#)]
19. Zambrano-Mera, D.F.; Broens, M.I.; Villarreal, R.; Espinoza-Gonzalez, R.; Aguilar-Hurtado, J.Y.; Wang, B.; Suarez, S.; Mücklich, F.; Valenzuela, P.; Gacitúa, W.; et al. Solid Lubrication Performance of Sandwich Ti<sub>3</sub>C<sub>2</sub>T<sub>x</sub>-MoS<sub>2</sub> Composite Coatings. *Appl. Surf. Sci.* **2023**, *640*, 158295. [[CrossRef](#)]
20. Mohan, M.; Shetti, N.P.; Aminabhavi, T.M. Recent Developments in MoS<sub>2</sub>-Based Flexible Supercapacitors. *Mater. Today Chem.* **2023**, *27*, 101333. [[CrossRef](#)]
21. Yazyev, O.V.; Kis, A. MoS<sub>2</sub> and Semiconductors in the Flatland. *Mater. Today* **2015**, *18*, 20–30. [[CrossRef](#)]
22. Wu, Z.-S.; Zhou, G.; Yin, L.-C.; Ren, W.; Li, F.; Cheng, H.-M. Graphene/Metal Oxide Composite Electrode Materials for Energy Storage. *Nano Energy* **2012**, *1*, 107–131. [[CrossRef](#)]
23. Jose, S.P.; Tiwary, C.S.; Kosolwattana, S.; Raghavan, P.; Machado, L.D.; Gautam, C.; Prasankumar, T.; Joyner, J.; Ozden, S.; Galvao, D.S.; et al. Enhanced Supercapacitor Performance of a 3D Architecture Tailored Using Atomically Thin rGO–MoS<sub>2</sub> 2D Sheets. *RSC Adv.* **2016**, *6*, 93384–93393. [[CrossRef](#)]
24. Kelly, P.J.; Arnell, R.D. Magnetron Sputtering: A Review of Recent Developments and Applications. *Vacuum* **2000**, *56*, 159–172. [[CrossRef](#)]
25. Ekpe, S.D.; Jimenez, F.J.; Field, D.J.; Davis, M.J.; Dew, S.K. Effect of Magnetic Field Strength on Deposition Rate and Energy Flux in a Dc Magnetron Sputtering System. *J. Vac. Sci. Technol. A Vac. Surf. Film.* **2009**, *27*, 1275–1280. [[CrossRef](#)]
26. Lu, X.; Sui, X.; Niu, D.; Yan, Z.; Cao, X.; Hao, J.; Liu, W. Exploring the Effect of V Doping on the Tribological Mechanism of MoS<sub>2</sub> Coatings in Atomic Oxygen Environment. *Mater. Today Commun.* **2023**, *36*, 106721. [[CrossRef](#)]
27. Wu, C.-R.; Chang, X.-R.; Wu, C.-H.; Lin, S.-Y. The Growth Mechanism of Transition Metal Dichalcogenides by Using Sulfurization of Pre-Deposited Transition Metals and the 2D Crystal Hetero-Structure Establishment. *Sci. Rep.* **2017**, *7*, 42146. [[CrossRef](#)] [[PubMed](#)]
28. Wu, C.-R.; Chang, X.-R.; Chu, T.-W.; Chen, H.-A.; Wu, C.-H.; Lin, S.-Y. Establishment of 2D Crystal Heterostructures by Sulfurization of Sequential Transition Metal Depositions: Preparation, Characterization, and Selective Growth. *Nano Lett.* **2016**, *16*, 7093–7097. [[CrossRef](#)] [[PubMed](#)]
29. Chen, K.-C.; Chu, T.-W.; Wu, C.-R.; Lee, S.-C.; Lin, S.-Y. Layer Number Controllability of Transition-Metal Dichalcogenides and the Establishment of Hetero-Structures by Using Sulfurization of Thin Transition Metal Films. *J. Phys. D Appl. Phys.* **2017**, *50*, 064001. [[CrossRef](#)]
30. Wang, W.; Shen, H.; Jiang, F.; He, X.; Yue, Z. Low-Cost Chemical Fabrication of Cu<sub>2</sub>ZnSnS<sub>4</sub> Microparticles and Film. *J. Mater. Sci. Mater. Electron.* **2013**, *24*, 1813–1817. [[CrossRef](#)]
31. Wang, W.; Wang, G.; Chen, G.; Chen, S.; Huang, Z. The Effect of Sulfur Vapor Pressure on Cu<sub>2</sub>ZnSnS<sub>4</sub> Thin Film Growth for Solar Cells. *Solar Energy* **2017**, *148*, 12–16. [[CrossRef](#)]
32. Mihai, C.; Sava, F.; Simandan, I.D.; Galca, A.C.; Burducea, I.; Becherescu, N.; Velea, A. Structural and Optical Properties of Amorphous Si–Ge–Te Thin Films Prepared by Combinatorial Sputtering. *Sci. Rep.* **2021**, *11*, 11755. [[CrossRef](#)] [[PubMed](#)]
33. Haynes, W.M. *CRC Handbook of Chemistry and Physics*, 95th ed.; CRC Press: Hoboken, NJ, USA, 2014; ISBN 9781482208689.
34. Frey, G.L.; Tenne, R.; Matthews, M.J.; Dresselhaus, M.S.; Dresselhaus, G. Raman and Resonance Raman Investigation of MoS<sub>2</sub> Nanoparticles. *Phys. Rev. B* **1999**, *60*, 2883–2892. [[CrossRef](#)]
35. Li, H.; Zhang, Q.; Yap, C.C.R.; Tay, B.K.; Edwin, T.H.T.; Olivier, A.; Baillargeat, D. From Bulk to Monolayer MoS<sub>2</sub>: Evolution of Raman Scattering. *Adv. Funct. Mater.* **2012**, *22*, 1385–1390. [[CrossRef](#)]
36. Chen, J.M.; Wang, C.S. Second Order Raman Spectrum of MoS<sub>2</sub>. *Solid State Commun.* **1974**, *14*, 857–860. [[CrossRef](#)]
37. Livneh, T.; Spanier, J.E. A Comprehensive Multiphonon Spectral Analysis in MoS<sub>2</sub>. *2D Mater.* **2015**, *2*, 035003. [[CrossRef](#)]

38. Carvalho, B.R.; Wang, Y.; Mignuzzi, S.; Roy, D.; Terrones, M.; Fantini, C.; Crespi, V.H.; Malard, L.M.; Pimenta, M.A. Intervalley Scattering by Acoustic Phonons in Two-Dimensional MoS<sub>2</sub> Revealed by Double-Resonance Raman Spectroscopy. *Nat. Commun.* **2017**, *8*, 14670. [[CrossRef](#)]
39. Chakraborty, B.; Matte, H.S.S.R.; Sood, A.K.; Rao, C.N.R. Layer-dependent Resonant Raman Scattering of a Few Layer MoS<sub>2</sub>. *J. Raman Spectrosc.* **2013**, *44*, 92–96. [[CrossRef](#)]
40. Mignuzzi, S.; Pollard, A.J.; Bonini, N.; Brennan, B.; Gilmore, I.S.; Pimenta, M.A.; Richards, D.; Roy, D. Effect of Disorder on Raman Scattering of Single-Layer Mo S<sub>2</sub>. *Phys. Rev. B* **2015**, *91*, 195411. [[CrossRef](#)]
41. Chen, W.; Gui, X.; Yang, L.; Zhu, H.; Tang, Z. Wrinkling of Two-Dimensional Materials: Methods, Properties and Applications. *Nanoscale Horiz.* **2019**, *4*, 291–320. [[CrossRef](#)]
42. Sava, F.; Simandan, I.-D.; Buruiana, A.-T.; Bocirnea, A.E.; El Khouja, O.; Tite, T.; Zaki, M.Y.; Mihai, C.; Velea, A. Synthesis of WS<sub>2</sub> Ultrathin Films by Magnetron Sputtering followed by Sulfurization in a Confined Space. *Surfaces* **2024**, *7*, 108–119. [[CrossRef](#)]
43. Tang, L.A.L.; Lee, W.C.; Shi, H.; Wong, E.Y.L.; Sadovoy, A.; Gorelik, S.; Hobley, J.; Lim, C.T.; Loh, K.P. Highly Wrinkled Cross-Linked Graphene Oxide Membranes for Biological and Charge-Storage Applications. *Small* **2012**, *8*, 423–431. [[CrossRef](#)] [[PubMed](#)]
44. Liu, Y.-Z.; Chen, C.-M.; Li, Y.-F.; Li, X.-M.; Kong, Q.-Q.; Wang, M.-Z. Crumpled Reduced Graphene Oxide by Flame-Induced Reduction of Graphite Oxide for Supercapacitive Energy Storage. *J. Mater. Chem. A* **2014**, *2*, 5730–5737. [[CrossRef](#)]
45. Song, Y.; Cheng, X.; Chen, H.; Huang, J.; Chen, X.; Han, M.; Su, Z.; Meng, B.; Song, Z.; Zhang, H. Integrated Self-Charging Power Unit with Flexible Supercapacitor and Triboelectric Nanogenerator. *J. Mater. Chem. A* **2016**, *4*, 14298–14306. [[CrossRef](#)]
46. Qi, D.; Liu, Z.; Liu, Y.; Leow, W.R.; Zhu, B.; Yang, H.; Yu, J.; Wang, W.; Wang, H.; Yin, S.; et al. Suspended Wavy Graphene Microribbons for Highly Stretchable Microsupercapacitors. *Adv. Mater.* **2015**, *27*, 5559–5566. [[CrossRef](#)] [[PubMed](#)]
47. Yu, X.; Wang, Y.; Li, L.; Li, H.; Shang, Y. Soft and Wrinkled Carbon Membranes Derived from Petals for Flexible Supercapacitors. *Sci. Rep.* **2017**, *7*, 45378. [[CrossRef](#)] [[PubMed](#)]
48. Zang, X.; Zhu, M.; Li, X.; Li, X.; Zhen, Z.; Lao, J.; Wang, K.; Kang, F.; Wei, B.; Zhu, H. Dynamically Stretchable Supercapacitors Based on Graphene Woven Fabric Electrodes. *Nano Energy* **2015**, *15*, 83–91. [[CrossRef](#)]
49. Li, X.; Zhao, T.; Chen, Q.; Li, P.; Wang, K.; Zhong, M.; Wei, J.; Wu, D.; Wei, B.; Zhu, H. Flexible All Solid-State Supercapacitors Based on Chemical Vapor Deposition Derived Graphene Fibers. *Phys. Chem. Chem. Phys.* **2013**, *15*, 17752. [[CrossRef](#)] [[PubMed](#)]
50. Chen, T.; Xue, Y.; Roy, A.K.; Dai, L. Transparent and Stretchable High-Performance Supercapacitors Based on Wrinkled Graphene Electrodes. *ACS Nano* **2014**, *8*, 1039–1046. [[CrossRef](#)]
51. Zhou, M.; Cai, T.; Pu, F.; Chen, H.; Wang, Z.; Zhang, H.; Guan, S. Graphene/Carbon-Coated Si Nanoparticle Hybrids as High-Performance Anode Materials for Li-Ion Batteries. *ACS Appl. Mater. Interfaces* **2013**, *5*, 3449–3455. [[CrossRef](#)]
52. Zhao, Y.; Feng, J.; Liu, X.; Wang, F.; Wang, L.; Shi, C.; Huang, L.; Feng, X.; Chen, X.; Xu, L.; et al. Self-Adaptive Strain-Relaxation Optimization for High-Energy Lithium Storage Material through Crumpling of Graphene. *Nat. Commun.* **2014**, *5*, 4565. [[CrossRef](#)] [[PubMed](#)]
53. Song, J.; Yu, Z.; Gordin, M.L.; Wang, D. Advanced Sulfur Cathode Enabled by Highly Crumpled Nitrogen-Doped Graphene Sheets for High-Energy-Density Lithium–Sulfur Batteries. *Nano Lett.* **2016**, *16*, 864–870. [[CrossRef](#)] [[PubMed](#)]

**Disclaimer/Publisher’s Note:** The statements, opinions and data contained in all publications are solely those of the individual author(s) and contributor(s) and not of MDPI and/or the editor(s). MDPI and/or the editor(s) disclaim responsibility for any injury to people or property resulting from any ideas, methods, instructions or products referred to in the content.